Spatial diversity control law for demultiplexer and active photonic integrated circuits for atmospheric effect mitigation

Yann Lucas, Vincent Michau, Serge Meimon

Spatial diversity control law for demultiplexer and active photonic integrated circuits for atmospheric effect mitigation

Yann Lucas[1,2], Vincent Michau[1], and Serge Meimon[1]

[1]DOTA, ONERA, Université de Paris-Saclay, 92320, Châtillon, France
[2]CNES, 75001, Paris, France

ABSTRACT

Free-space optical links theoretically allow very high-speed data rates. As the beams propagate through the atmosphere, the effects of turbulence introduce fading. To mitigate these effects, adaptive optics is commonly implemented. Recently, a spatial demultiplexer coupled to an active integrated photonic circuit has been proposed as a more compact solution to replace the adaptive optics device. This solution has been the subject of several demonstrations. In these demonstrations, the control of the photonic circuit is carried out by modulation or by criterion minimization. These techniques are demanding in terms of modulation bandwidth, particularly when the number of spatial modes to be corrected increases. We propose a control method allowing the increase of the number of corrected modes without increasing the modulation bandwidth. This control method is based on a spatial coding of the modulation, also called spatial diversity. Unlike state-of-the-art techniques in which modes are controlled sequentially, with spatial diversity, all the modes are controlled at the same time. Spatial diversity closed loop stability is demonstrated in a numerical simulation.

Keywords: Integrated optics, optical communication, coherent combining, spatial modulation, wavefront sensing

1. INTRODUCTION

Mitigating atmospheric effects on the laser beam propagation is mandatory to reach very high-speed data rates allowed by free-space optical links. Adaptive optics can be used to mitigate these effects. On the other hand, it is a bulky solution, complex to implement, and it shows efficiency limitations on strongly perturbed beams.[1,2] Alternatively, a more compact and robust solution, also enabling correction in strong perturbation regime has been proposed. In such a solution, the perturbed field is decomposed in a set of guided waves which are added coherently in a Photonic Integrated Circuit (PIC) with active phase shifters. The concept was first proposed by N.Schwartz in ref.[3] The number of guided waves to be coherently combined by the PIC is close to the number of modes of adaptive optics. It can reach several tens, even hundreds, depending on the diameter of the receiver and on the Fried parameter.[4]

To achieve the coherent combination, the PIC phase shifters are controlled in real time. State-of-the-art control algorithms used for PIC real-time control are either based on phase shifter temporal/frequency modulation, or hill-climbing algorithms such as the SPGD/ASPGD, or the Nelder-Mead algorithm. The main advantage of hill climbing methods is their robustness when locking the control loop. On the other hand, once close to the optimum, their temporal behavior cannot be better than an optimized modulation. Stochastic Parallel Gradient Descent (SPGD)[5] or Adam-SPGD (ASPG)[6] algorithm has been applied for maximizing of the constructive PIC output (the telecom signal dedicated output). In that case, the modulation control is applied phase-shifter per phase-shifter. The classical modulation techniques have been also implemented by using the constructive PIC output only with a control phase-shifter per phase-shifter done sequentially, or with multi-dither.[7–10] Depending on the recombination architectures of the PICs, it is possible to have access to destructive outputs, hence separating the different phase shifters modulations within a recombination stage of the PIC. The sequential or

Further author information:
yann.lucas@onera.fr

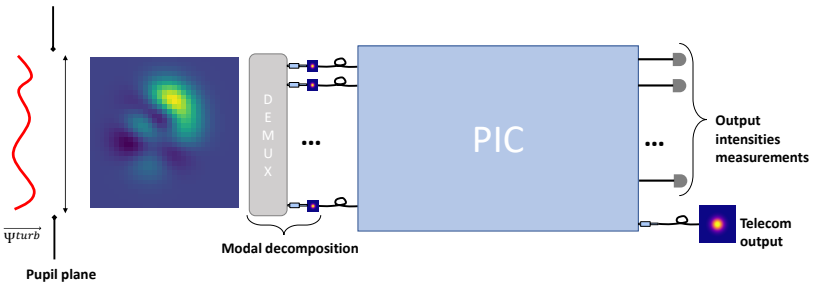

Figure 1. Architecture of a PIC coherent combining device for atmospheric effect mitigation

frequency modulations can then be used to separate the modulations of sets of stage grouped phase shifters, in order to reduce the required modulation bandwidth. Finally, the Nelde-Mead algorithm has been applied stage by stage using all output measurements in one stage.[11]

Unlike an adaptive optics system in which the complete correction is done in one step, these methods lead to correction by phase shifters or by groups of phase shifters. They therefore require phase shifters with a modulation bandwidth much higher than that required for correcting the effects of atmospheric turbulence. This requirement is all the stronger as the number of modes to be corrected is high. At the same time, depending on the technology on which the manufacturing of PICs is based, the response time of the phase shifters is limited. In the case of Si technology which allows the most complex PICs, therefore well suited to the correction of a high number of modes, the most common phase shifters are thermal phase shifters which have response times of the order of ten microseconds.

We propose and study here an alternative method which relies on a single modulation for the determination of all the phase shifts. This method makes it possible to consider the coherent combination of a high number of modes without a significant increase in the modulation bandwidth. The spatial diversity control method was first developed by L. Rinaldi,[12] for the control of a deformable mirror from signals in the focal plane. In the present case, the set of phase shifters play the role of a deformable mirror and the output signals from the PIC take the place of the signals at the focal plane. The spatial diversity algorithm allows the PIC to be used to perform a kind of wavefront measurement in a single step. It then allows control of all modes simultaneously. In section 2, we present the PIC-based coherent combining device for mitigating the effects of atmospheric turbulence and define some useful notions for the following parts. In section 3, we present the principle of the spatial diversity algorithm and show its performance as a wavefront sensor. Finally, in section 4, we implement a spatial diversity control law in an E2E simulation and show its ability to close the loop as well as its stability.

2. PIC BASED COHERENT COMBINING DEVICE

2.1 Architecture

A coherent combining system based on a PIC is composed of two stages (see Figure 1). The first stage, the spatial demultiplexer, is passive. The demultiplexer decomposes the incident wave into a set of single-mode waves propagating in optical guides. The second stage, the photonic circuit, includes active phase shifters to allow the coherent and constructive combination of these signals. The main PIC output, called coherent output or telecom output, corresponds to the coherent sum (constructive interference) of the guided waves injected at the PIC input. Secondary outputs provide access to different states of destructive interference between guided waves: they are used to control the PIC phase shifters. The whole process is equivalent to single mode fiber (SMF) injection with adaptive optics.[13]

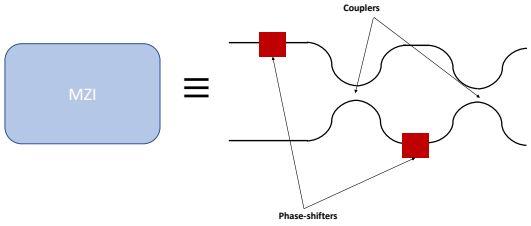

Figure 2. Active Mach-Zehnder interferometer

2.2 Spatial demultiplexer

Let $\boldsymbol{\Psi_{turb}}$ be the complex amplitude of the optical field received in the pupil plane telescope after atmospheric propagation. A spatial demultiplexer performs the decomposition of $\boldsymbol{\Psi^{turb}}$ as:

$$\boldsymbol{\Psi_{turb}} = \sum_{i=0}^{N-1} (\boldsymbol{\Psi_{turb}}.\boldsymbol{Mod_i})\boldsymbol{Mod_i} + \boldsymbol{\Psi_\infty}\,, \tag{1}$$

where $(\boldsymbol{Mod_i})$ is a set of N orthonormal modes of propagation. The '.' symbolizes the scalar product. The set of modes depends on the demultiplexer. It may be Hermite-Gaussian modes by using a Multi-Plan Light Convertion (MPLC),[14,15] Laguerre-Gaussian modes by using a photonic lantern,[16,17] or Fourier modes by using a microlens array.[18,19]

At the output of the demultiplexer, the N complex amplitudes of the guided waves are represented by (a_i), where $a_i = \boldsymbol{\Psi^{turb}}.\boldsymbol{Mod_i}$.

2.3 PIC coherent combining

Let us examine some PIC architectures to achieve such a coherent combining.

An active Mach-Zehnder interferometer (MZI) allows the combination of two coherent waves of different amplitude and phase without loss of power. An active MZI comprises of two couplers and two phase-shifters (see Figure 2). The first phase-shifter/coupler stage balances amplitude between two beams, and enables the second phase-shifter/coupler stage performing the lossless combination (see demonstration in Appendix A).

Figure 3 presents a combination architecture for the addition of N guided waves. At each stage, the guided waves are combined two by two using an active MZI. The guided waves coming from the constructive outputs are injected in the inputs of the next stage, while the guided waves from the destructive outputs are directed to optical detectors. This architecture, called here geometrical, minimizes the number of couplers and phase shifters seen by the guided waves and therefore the losses induced by these components. By considering a lossless PIC, the power of guided wave at the constructive output of such a architecture (telecom output) equals the sum of the powers of the N guided waves injected into the PIC:

$$s_{tot} = \sum_{i=0}^{N-1} |a_i|^2\,. \tag{2}$$

In the following, the constructive output is designated by the index 0.

Unfortunately, due to a lack of technological maturity, the losses encountered in the PICs currently supplied by the founders are significant.[20–23] Reducing the number of functions seen by the guided waves in the PIC is one way to reduce these losses. We therefore also consider here a recombination architecture where only the phases of the guided waves are corrected. Such an architecture is described in Figure 4.

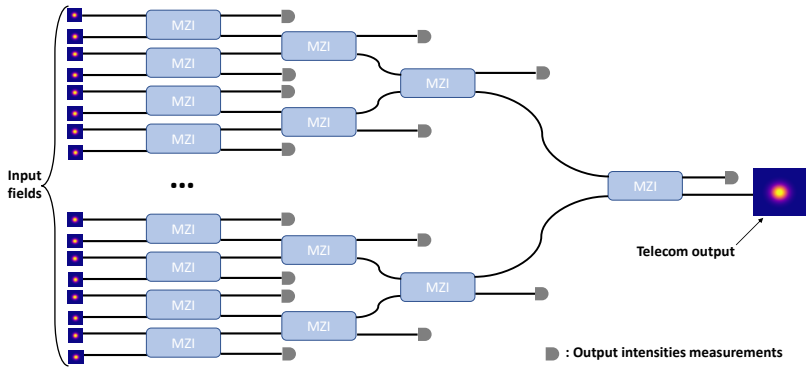

Figure 3. Geometrical architecture enabling phase and amplitude correction

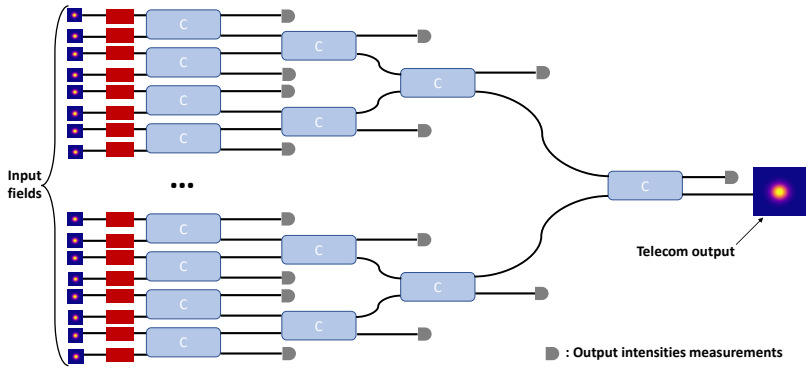

Figure 4. Geometrical architecture enabling phase-only correction (C denotes a simple coupler)

Note that, with this simplified architecture, the number of couplers and phase shifters involved in the the guided wave propagation is divided by two compared to the previous architecture (see Figures 3 and 4). The recombined signal then writes

$$s_{p-o} = |\frac{1}{N}\sum_{i=0}^{N-1} a_i|^2 \,, \tag{3}$$

is reduced, s_{p-o} only reaching s_{tot} in the case where all the amplitudes of the guided waves are equal. This attenuation depends on the statistics governing the amplitudes of the input waves. When the amplitudes follow the same statistic, the mean attenuation may be expressed in two cases of interest, i.e. the lognormal statistic:

$$< s_{p-o} >_{lognormal} = e^{-\sigma^2_{ln(a)}} < s_{tot} > \,, \tag{4}$$

and the Rayleigh statistic:

$$< s_{p-o} >_{Rayleigh} = \frac{\pi}{4} < s_{tot} > \,. \tag{5}$$

2.4 Phase corrector control

The problem of controlling the phase shifters comes down to determining the values to apply to the PIC phase-shifters in order to maximize the power on the telecom output, given the powers measured on all the outputs.

We note $\boldsymbol{a} = (a_i)$, the vector of the complex amplitudes of the guided waves at the input of the PIC, this vector being identified for simplicity with the outputs of the multiplexer, and $\boldsymbol{b} = (b_j)$, the vector of the complex amplitudes of the guided waves at the output of the PIC. The index $j = 0$ designates the telecom output. The PICs considered here only integrate phase shifters and couplers which are linear operators. We can therefore write:

$$\boldsymbol{b} = \boldsymbol{M_{pic}}\boldsymbol{a}\,. \tag{6}$$

In Equation 6, $\boldsymbol{M_{pic}}$ is a function of the architecture of the PIC but also of the vector of phases introduced by the phase shifters ,$\boldsymbol{\varphi_{corr}} = (\varphi_{corr_k})$. $\boldsymbol{M_{pic}}$ is therefore a matrix which evolves over time. In the case of the architecture dedicated to phase correction alone, it is possible to write $\boldsymbol{M_{pic}}$ as the product of two matrices:

$$\boldsymbol{M_{pic}} = \boldsymbol{M_c}\boldsymbol{M_{corr}}\,. \tag{7}$$

$\boldsymbol{M_c}$ describes wave combining. It is a constant matrix depending on the architecture of the PIC. $\boldsymbol{M_{corr}}$ describes the correction by the phase shifters: it is a diagonal matrix, with diagonal element $e^{j\varphi_{corr_i}}$. Finally, the measured quantities are :

$$s_j = |b_j|^2. \tag{8}$$

The problem that arises is therefore to determine φ_{corr} which maximizes $|b_0|^2$, knowing the measures of $\boldsymbol{s} = (s_j)$. In the case of adaptive optics, the measured quantities are generally linear functions of the correction phases induced by the deformable mirror. The inverse problem is relatively easy. In the present case, the measured quantities, s_j, are quadratic functions of the phasors $e^{\varphi_{corr_k}}$. The modulation technique makes it possible to overcome this difficulty. The differential signal, $\Delta s(\varphi) = s(\varphi + \delta\varphi_m) - s(\varphi - \delta\varphi_m)$, measured in the presence of modulation $\delta\varphi_m$ gives access to the derivative of the signal. Near the optimum, φ_{opt}, this derivative is a linear function of the phase error and can therefore be used as an error signal:

$$s(\varphi) = \frac{1}{2}\frac{\partial^2 s}{\partial\varphi^2}(\varphi_{opt}) \times \varphi^2, \tag{9}$$

where φ represents the distance from the optimum in phase space. Then:

$$\Delta s(\varphi) = \left[2\frac{\partial^2 s}{\partial\varphi^2}(\varphi_{opt}) \times \delta\varphi_m\right]\varphi. \tag{10}$$

This method introduced in the case of a single phase shifter can easily be generalized to the case of any number of phase shifters with sequential or multi-frequency modulations. However, it suffers from several limitations. With sequential or multi-frequency modulation, the modulation frequency is dependent on the number of phase shifters to be corrected. For a high number of phase shifters, the required modulation frequency can be higher than the maximum reachable phase shifter frequency due to technological limitations. Furthermore, The phase error must be almost constant during modulation, which requires rapid modulation with regards to the evolution time of the turbulence effects. $\frac{\partial^2 s}{\partial\varphi^2}(\varphi_{opt})$ depends on the respective amplitudes of the interfering waves: in a closed loop, variations in these amplitudes introduce variations in the gain of the loop. Finally, this method is only valid near the maximum, which poses the problem of locking the control loop.

We study this method and its limitations in more complex context with a spatially encoded modulation.

3. SPATIAL DIVERSITY DITHERING

3.1 Principle

Instead of encoding the modulation temporally or in frequency, we encode the modulation spatially. By denoting $\boldsymbol{\delta\varphi_m} = (\delta\varphi_{m_j})$, the vector of spatial phase modulation, and $\boldsymbol{\Delta s} = (\Delta s_j)$, the vector of differential measurements, where $\Delta s_j(\boldsymbol{\varphi}) = s_j(\boldsymbol{\varphi} + \boldsymbol{\delta\varphi_m}) - s_j(\boldsymbol{\varphi} - \boldsymbol{\delta\varphi_m})$, we obtain a linear relationship between $\boldsymbol{\varphi}$ and $\boldsymbol{\Delta s}$ (see demonstration in Appendix B):

$$\boldsymbol{\Delta s} = \boldsymbol{M_{\delta\varphi_m}}\boldsymbol{\varphi} \tag{11}$$

As in the one-dimensional case, the matrix depends on the modulation vector, $\boldsymbol{\delta\varphi_m}$, but also on the amplitudes of the input guided waves, ($|a_i|$). Assuming independent uniform additive noise on the measurements, the phases can be estimated using the least squares. The phase estimate is written:

$$\hat{\boldsymbol{\varphi}} = \boldsymbol{M}^{\dagger}_{\boldsymbol{\delta\varphi_m}} \boldsymbol{\Delta s}\,, \tag{12}$$

where $\boldsymbol{M}^{\dagger}_{\boldsymbol{\delta\varphi_m}}$ represents the generalized inverse of $\boldsymbol{M}_{\boldsymbol{\delta\varphi_m}}$.

With this algorithm, named spatial diversity, the modulation is encoded spatially rather than temporally. All output measurements are used in the same time to estimate the phase error and control all the phase-shifters in one step.

In practice, in the case of the architecture allowing phase correction only, the number of measurements equals the number of phase shifters. The matrix $\boldsymbol{M}^{\dagger}_{\boldsymbol{\delta\varphi_m}}$ is square and we can hope that the inversion allows all the phase values to be estimated. In the case of the architecture allowing phase and amplitude correction, the phase shifters are twice as numerous as the measurements. The inversion will not be able to estimate all the phase values from a single vector of measurements. In the latter case, it is necessary to consider the successive recording of two series of measurements with two different spatial modulations.

In presence of additive noise, $\boldsymbol{\Delta n} = (\Delta n_i)$ on the differential measurements, the phase estimation in equation 12 becomes:

$$\hat{\boldsymbol{\varphi}} = \boldsymbol{M}^{\dagger}_{\boldsymbol{\delta\varphi_m}} \boldsymbol{\Delta s} + \boldsymbol{M}^{\dagger}_{\boldsymbol{\delta\varphi_m}} \boldsymbol{\Delta n}\,, \tag{13}$$

The covariance matrix of estimated phase error, $\boldsymbol{\varphi_n}$, is:

$$< \boldsymbol{\varphi_n}^{t} \boldsymbol{\varphi_n} > = < \boldsymbol{M}^{\dagger}_{\boldsymbol{\delta\varphi_m}} \boldsymbol{C_{\Delta n}}^{\boldsymbol{t}} \boldsymbol{M}^{\dagger}_{\boldsymbol{\delta\varphi_m}} >\,, \tag{14}$$

The noise terms, Δn_i, are assumed to be centered, uniform and independent, of variance $\sigma^2_{\Delta n}$. The covariance matrix of differential measurement noise $\boldsymbol{C}_{\Delta n}$ equals $\sigma^2_{\Delta n}\mathbb{I}$, where $\mathbb{I}$ denotes the identity matrix :

$$< \boldsymbol{\varphi_n}^{t} \boldsymbol{\varphi_n} > = \sigma^2_{\Delta n} < \boldsymbol{M}^{\dagger}_{\boldsymbol{\delta\varphi_m}}{}^{t} \boldsymbol{M}^{\dagger}_{\boldsymbol{\delta\varphi_m}} >\,, \tag{15}$$

The whole quadratic error on the estimated phases is: $< |\boldsymbol{\varphi_n}|^2 > = tr < \boldsymbol{\varphi_n}^{t} \boldsymbol{\varphi_n} >$ By using the singular value decomposition of $\boldsymbol{M}_{\boldsymbol{\delta\varphi_m}}$, it comes:

$$\begin{aligned} < |\boldsymbol{\varphi_n}|^2 > &= \sigma^2_{\Delta n} tr(\boldsymbol{V}\boldsymbol{\Sigma}^{\boldsymbol{\dagger^2}}\boldsymbol{V}^{\boldsymbol{t}}) \\ &\propto \sigma^2_{\Delta n} \sum \frac{1}{V_s^2} \end{aligned}\,, \tag{16}$$

with V_s the singular values of $\boldsymbol{M}_{\boldsymbol{\delta\varphi_m}}$.

The noise propagation depends on the chosen spatial modulation vector $\boldsymbol{\delta\varphi_m}$. The interaction matrix must be well-conditioned to limit noise propagation so that its inversion does not amplify it.

3.2 A PIC as a wavefront sensor

In section 3.1, we introduced the principle of spatial diversity for phase estimation and discussed one of its limitations, the propagation of measurement noise. In this section, we are interested in the precision of phase estimation in the absence of measurement noise, i.e. the bias introduced by deviations from the quadratic model used in section 3.1.

The output signals are calculated according to the phases, called true phases, introduced by the phase shifters based on Eq. 7 and 8. The phases estimated from these output signals are then calculated from the inverse matrix (see Eq. 12).

This study is carried out in the case of the architecture allowing phase correction only (see Fig. 4). The photonic circuit has 32 inputs and 32 outputs. Referring to the architecture shown in Fig. 4, inputs as well as phase shifters are numbered in ascending order from top to bottom. We chose a very low amplitude modulation

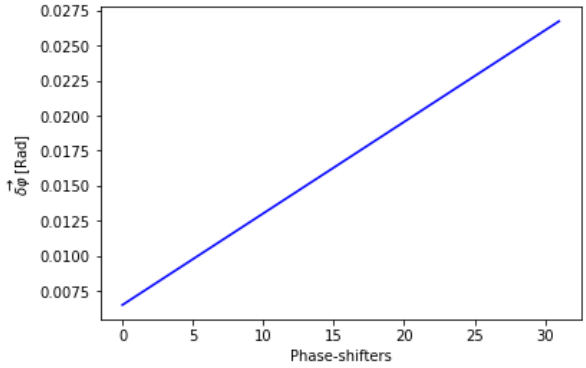

Figure 5. Phase tilt spatial modulation vector $\boldsymbol{\delta\varphi_m}$

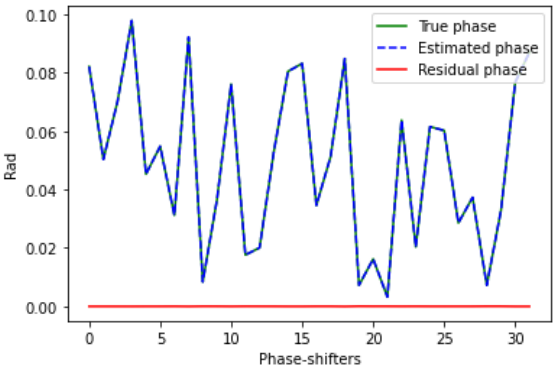

Figure 6. Spatial diversity phase estimation of a random perturbed phase lower than 0.1 rad

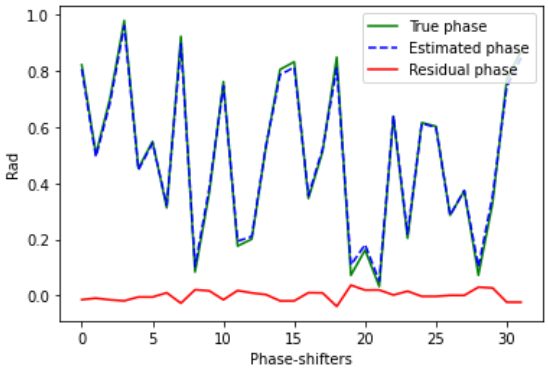

Figure 7. Spatial diversity phase estimation of a random perturbed phase lower than 1 rad

compared to the amplitudes of the phases to be estimated so that it does not disturb the estimation of the bias on these phases (see Fig. 5). The amplitudes of the input guided waves are assumed to be calibrated and identical. We verified that the form of the modulation (a linear function of the input number) leads to a well-conditioned interaction matrix, $\boldsymbol{M_{\delta\varphi_m}}$. During the measurement process, i.e. during modulation, the true phases are static. Finally, throughout this numerical experiment, the relative amplitudes of these phases are preserved. Only their absolute amplitudes vary.

Figure 6 and 7 show in blue dotted line the spatial diversity phase estimation, 'Estimated phase', of a random perturbed phase, 'True phase', in green. The residual phase, i.e. the difference between the estimated and true phases is plotted in red. The phase estimation is perfect for perturbed phases lower than 0.1 rad and starts to deteriorate for perturbed phases reaching 1 rad.

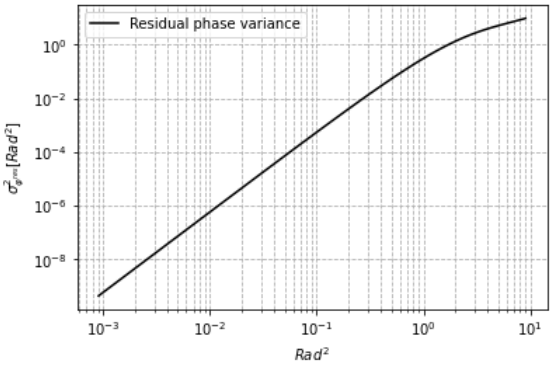

Figure 8. Spatial diversity phase estimation linear regime

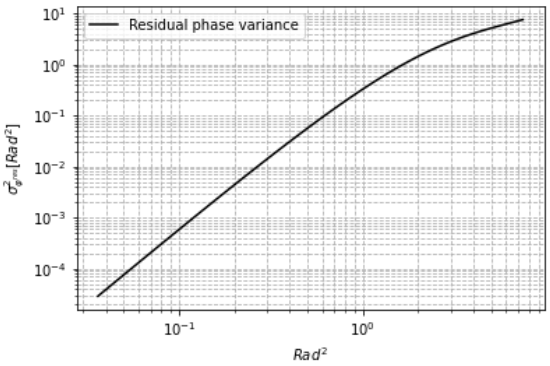

Figure 9. Spatial diversity phase estimation linear regime zoom around 1 rad^2

Figures 8 and 9 show the linear regime of the spatial diversity algorithm plotted as a residual phase estimation variance function of the amplitude of the perturbed phase.

As a conclusion, the spatial diversity algorithm enables to use the PIC as a wavefront sensor for perturbed phase variance up to 1 rad^2 with around 0.3 rad^2 residual phase variance precision. As expected, the dynamics of this method, restricted by the poor quadratic model; is low if compared to other wavefront sensors. On the other hand, it is enough for closed loop operation in case of low residual phases, i.e. in case of good correction. This method seems well-suited for optical communication which requires high level of atmospheric effect mitigation.

4. PIC CONTROL

4.1 Operating conditions

We carried out a numerical experiment to evaluate the possibility of using spatial diversity modulation for the control of the phase shifters of a PIC for the correction of atmospheric turbulence effects. The chosen scenario is that of a 1.5 μm optical downlink between a low-orbit satellite and a ground station.

The scenario is defined by the parameters characterizing the geometry of the beam between the satellite and the ground station, the optical propagation through atmospheric turbulence, and the diameter of the receiving telescope. We therefore choose the case of a satellite moving in the plane perpendicular to the plane of incidence of the beam on the telescope and we consider the case where the elevation of the receiving satellite-telescope axis is 30 deg. The C_n^2 profile is representative of an average daytime site, which leads to the following values for the propagation conditions:

- Fried parameter: $r_o = 10\ cm$ at 1.5 μm,
- Rytov variance: $\sigma_\chi^2 = 0,085$ at 1.5 μm.

The wind profile is a Bufton profile. Taking into account the satellite apparent trajectory, the natural wind is negligible compared to the apparent wind except for the first few hundred meters before the ground station: the mean windspeed is: $v_{moy} = 125\ m.s^{-1}$.

This scenario makes it possible to reveal field disturbances that are sufficiently complex to test the performance of a control loop while having the advantage of moderate complexity in terms of numerical modeling. It must, however, be emphasized that if we were to consider the implementation of a loop in a real case, a simple sequential modulation could be used given the limited number of modes to be corrected.

Optical propagation through the turbulent atmosphere is modeled with the PILOT code.[24]

A time sequence of the optical power collected by a 0.5 m telescope, $|\boldsymbol{\Psi_{turb}}|^2$, is shown in Figure 10. It can be observed that the retained diameter is sufficient to avoid deep fading. The complete assessment of the link including the transmitted power data is not given here: the characterization of the performance of the telecom link is not the subject of the study.

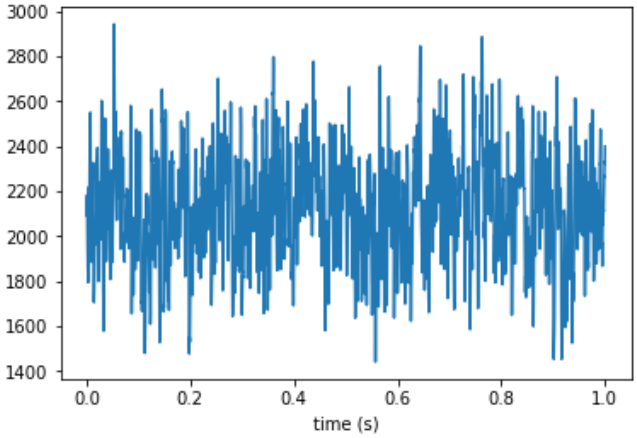

Figure 10. Time sequence of the optical power collected by the telescope (AU)

4.2 Performance analysis and dimensioning

The next step is the dimensioning of the system composed of a telescope, a multiplexer and an active PIC for the correction of the effects of atmospheric turbulence. We present a performance analysis to justify the choice of their parameters. As the strehl ratio is commonly used as a criterion in adaptive optics, we rely here on the normalized average of the power coupled into the telecom output to make a preliminary evaluation of the performance of the system:

$$\eta = \frac{< s_0 >}{< |\boldsymbol{\Psi_{turb}}|^2 >}$$

The presence of fading is also a criterion for a system dedicated to communications. We are therefore looking for a system with high coupled power, guarantee of limited fluctuation. At the same time, we calculated time sequences to check the fluctuation amplitude.

4.2.1 Spatial multiplexer

The average attenuation induced by the projection of the field onto a finite number of modes depends on the choice of the type of modes and the number of modes. Luca Rinaldi analytically calculated this attenuation for different families of modes.[4] In the following, we will assume a modal decomposition on 32 Hermite-Gauss modes. The analytical evaluation leads to an attenuation:

$$\eta_{demux} = \frac{< s_{tot} >}{< |\boldsymbol{\Psi_{turb}}|^2 >} = 0.65.$$

We projected a temporal sequence of fields created with the Turandot code onto a set of 32 Hermite-Gauss modes. The average attenuation value of s_{tot}, estimated from this sequence, 0.64, is very close to that obtained analytically. The temporal sequence of s_{tot} obtained from that sequence, as presented in the Figure 11, highlights the fades expected with such a number of modes.

The instantaneous signal given by recombination of the guided waves using a phase-only correction, s_{p-o} is plotted in Figure 12. The mean attenuation induced by the phase-only correction with regards to the total power is:

$$\eta_{p-o} = \frac{< s_{p-o,0} >}{< |\boldsymbol{\Psi_{turb}}|^2 >} = 0.48.$$

The attenuation induced by phase-only recombination, $\frac{0.48}{0.64} = 0.75$, is close to $\frac{\pi}{4}$, the expected value with fluctuations described by a Rayleigh distribution.

We have just characterized the fluctuations and attenuations induced by the first three stages of the system. The total attenuation of these three stages can be written as the product of the attenuations, making the simplifying assumption that the fluctuations are uncorrelated. This approach gives a preliminary evaluation

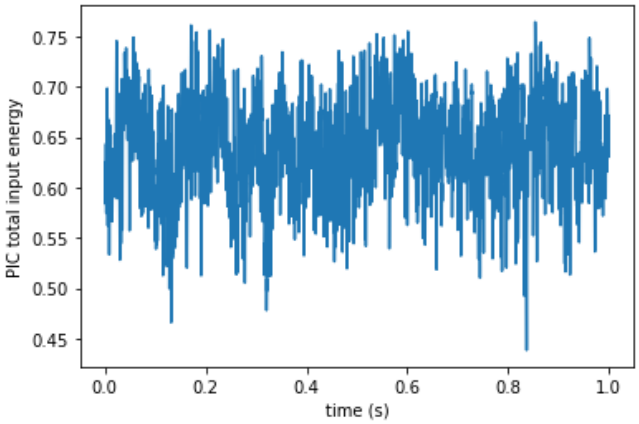

Figure 11. Time sequence of the optical power collected by 32 modes, time step is 6 µs

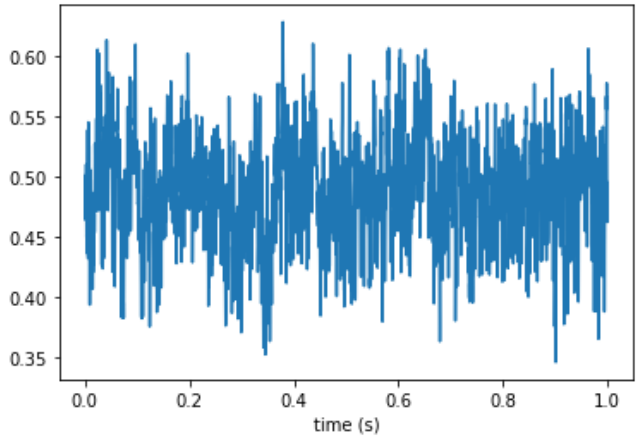

Figure 12. Time sequence of the optical power after phase-only recombination of 32 modes, time step is 6 µs

of the performance of our system by taking into account only its static properties. It remains to take into consideration the effects of the dynamic properties of the system, that is to say the active correction. In this preliminary analysis, we will also study this last floor independently for the sake of simplicity.

4.2.2 Active combination

The active recombination error has two origins: on the one hand, the measurement error which propagates over the control phase, and on the other hand, the temporal error linked to the control.

For the sake of simplicity and to be able to characterize these two sources of error separately, we consider the following sequence illustrated in Figure 13. The correction is renewed at time intervals of duration τ_c. During one time interval defined by two new corrections, the applied correction is constant and measurements are carried out by modulation. We denote τ_m as the modulation period. During a time interval between two corrections, $p = \frac{\tau_c}{\tau_m}$ measurements are carried out. The new correction is calculated by assuming a simple integrator with a gain of 0.5 from the average of the measurements carried out by modulation during the time interval preceding this new correction. The delay induced by the calculation time of the new correction is neglected in numerical modeling.

The temporal error can be roughly evaluated using the approach developed for adaptive optics. We therefore write the attenuation of the output signal as:

$$\eta_{tempo} = e^{-\sigma^2_{tempo}},$$

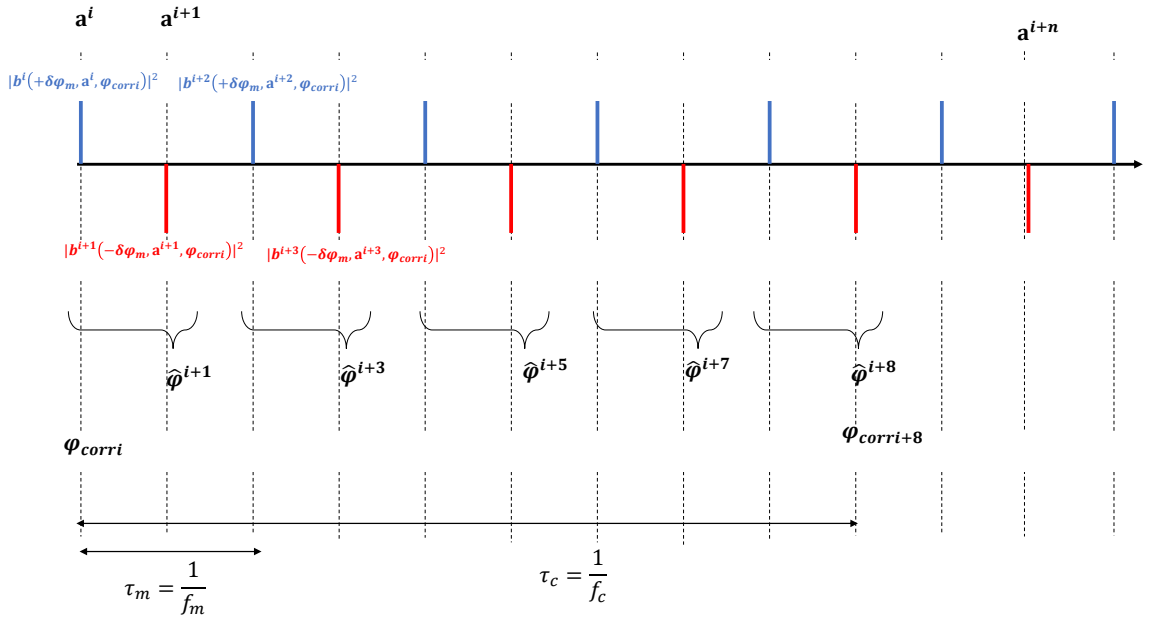

Figure 13. E2E close loop sequence

with :

$$\sigma^2_{tempo} = 6.88 \left(\frac{v_{moy}\tau_c}{r_o} \right)^{\frac{5}{3}} \ rad^2, \tag{17}$$

where v_{moy} is the average transverse windspeed. Assuming a control rate, $f_c = 12\ kHz$, i.e. $\tau_c = 0.08\ ms$, $\eta_{tempo} = 0.86$.

The measurement errors have several origins. We have already mentioned measurement noise. Having previously assumed the signal to be sufficiently powerful, we will consider here that the influence of detection noise can be neglected. In addition, the measurement model is based on two assumptions which are not fully verified in practice. On the one hand, as shown in appendix B, the interaction matrix was established by assuming that the amplitudes of the input guided waves are equal while it is a function of the amplitude PIC input fields and : any fluctuation of these amplitudes generates an error on matrix $\boldsymbol{M_{\delta\varphi_m}}$ (in fact on $\boldsymbol{M_{corr}}$), therefore on $\boldsymbol{M^{\dagger}_{\delta\varphi_m}}$ and hence on $\hat{\boldsymbol{\varphi}}$. On the other hand, it assumed that the phase to be measured is constant during modulation.

Let us examine the consequence of this last hypothesis. We assume the signal sampled at frequency $f_m = \frac{1}{2\tau_m}$. We denote by p the pth sample, and $\boldsymbol{\varphi_{turb}}$, the phase disturbance to be measured. The average of $\boldsymbol{\varphi_{turb}}$ during modulation is:

$$\boldsymbol{\varphi_{turb_{moy}}}(p) = \frac{\boldsymbol{\varphi_{turb}}(p) + \boldsymbol{\varphi_{turb}}(p+1)}{2}.$$

The differential measurement resulting from the modulation can be interpreted as a measurement obtained with a $\boldsymbol{\varphi_{turb_{moy}}}(p)$ disturbance and a modulation equal to $\boldsymbol{\delta\varphi_m} + \boldsymbol{\delta\varphi_{turb}}$, where:

$$\boldsymbol{\delta\varphi_{turb}}(p) = \frac{\boldsymbol{\varphi_{turb}}(p) - \boldsymbol{\varphi_{turb}}(p+1)}{2}.$$

This last error therefore also results in an error on the matrix $\boldsymbol{M^{\dagger}_{\delta\varphi_m}}$. Since the correction induced by the phase shifters is constant during modulation, $\boldsymbol{\varphi_{turb}}$ only depends on the complex amplitude of the guided waves at the

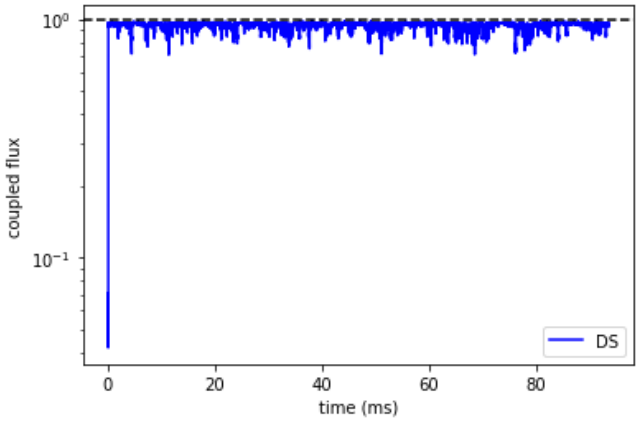

Figure 14. Telecom output intensity in closed loop: E2E simulation with temporal error only ($f_c = 12\ kHz$)

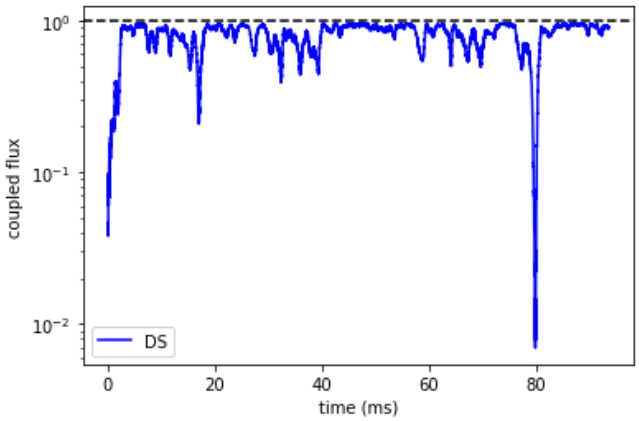

Figure 15. Telecom output intensity in closed loop: E2E simulation without phase variation during the modulation ($f_c = 12\ kHz$)

PIC input, like the previous error. On the other hand, unlike the latter, the modulation error impact depends on the modulation frequency and the modulation amplitude. Indeed, $\boldsymbol{\delta\varphi_{turb}}$ may be reduced by increasing f_m. Moreover, at constant $\boldsymbol{\delta\varphi_{turb}}$, the higher $\boldsymbol{\delta\varphi_m}$, the lower the relative modulation error. It is therefore this error which will determine the choice of frequency and modulation amplitude.

We studied the impact of these last two sources of error by numerical modeling. The errors induced by these two approximations are characterized separately in the end-to-end modeling presented in section

4.3 End-to-end modeling

The telecom output intensity, $|b_0|^2$, was first processed with the end-to-end simulation in case of a perfect correction applied at the frequency correction to validate the choice of $f_c = 12\ kHz$. $\frac{|b_0|^2}{s_{p-o}}$ is presented in Figure 14 . The average recombination efficiency is: $< \frac{|b_0|^2}{s_{p-o}} >= 0.94$ which is better than the rough value given by Eq. 17.

The telecom output intensity $|b_0|^2$ was then processed with the end-to-end simulation taking into account the estimated phase from the spatial diversity algorithm to compute the correction phase to be applied. First, to eliminate the effects due to phase variation during modulation, the modulation frequency is chosen as infinite. A constant gain in the interaction matrix approximates the mean of the amplitude fluctuations. The interaction matrix is a biased estimator for the perturbed phase, which degrades the algorithm's performance as seen in Figure 15. The average attenuation is then: 0.79.

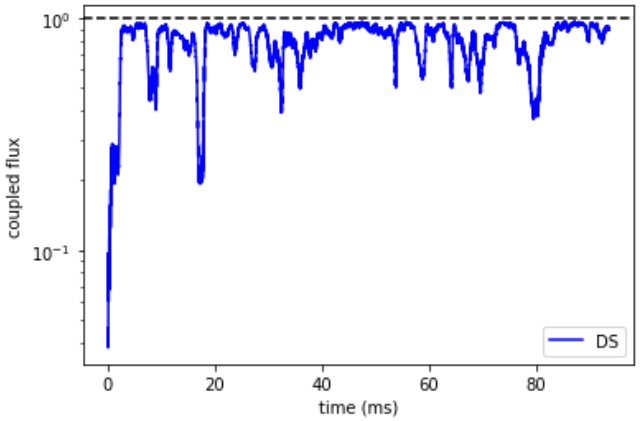

Figure 16. Telecom output intensity in closed loop: E2E simulation with input field amplitude fluctuation and phase variation during modulation ($f_c = 12\ kHz$, $f_m = 50\ kHz$)

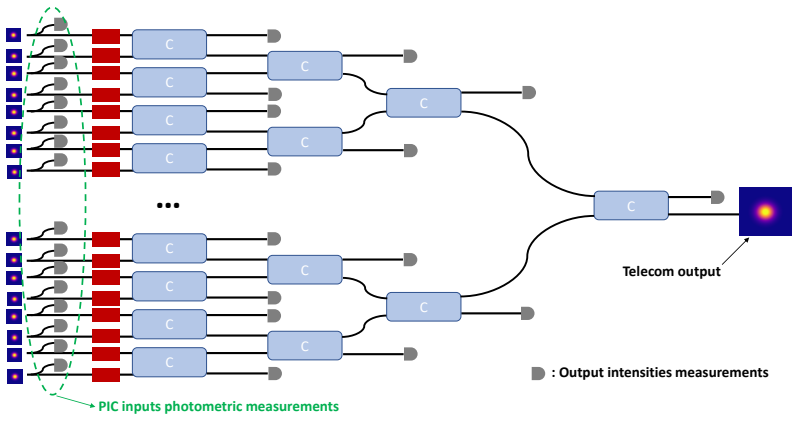

Figure 17. Geometrical architecture enabling phase-only correction with inputs photometric measurments

In Figure 16, $\frac{|b_0|^2}{s_{p-o}}$ is processed with the end-to-end simulation including all the effects on control loop (frequency modulation, f_m fixed at 50 kHz). The average efficiency is still 0.79 and the variance of its fluctuations 0.029. The behavior of the control loop is close to its behavior with amplitude fluctuations only. This confirms that the effects of amplitude variations are indeed preponderant on the loop. The effect of the fluctuation of the amplitudes of the guided waves are clearly predominant compared to temporal error and modulation error induced by phase fluctuations. To mitigate the effect of the fluctuation of the amplitudes of the guided waves, we propose to measure these amplitudes at the inputs of the PIC by detectors (see architecture presented in Figure 17). With such measurements, called photometric measurements by astronomers, it is possible to correct in real time the amplitude of the differential signal in order to approximate a signal measured in the absence of amplitude fluctuation. The interaction matrix $\boldsymbol{M}^{\dagger}_{\boldsymbol{\delta\varphi_m}}$ is updated with the photometric measurements at a frequency f_{pm}. We carried out a last simulation to illustrate the possible gain with such measurements. Results obtained with the end-to-end modeling are presented in Figure 18 for $f_{pm} = 1\ kHz$ with an average efficiency of 0.85 and a variance of its fluctuations of 0.029 and in Figure 19 for $f_{pm} = 4\ kHz$ with an average efficiency of 0.92 and a variance of its fluctuations of 0.01. Performances are clearly improved with regards to the results presented in Figure 16.

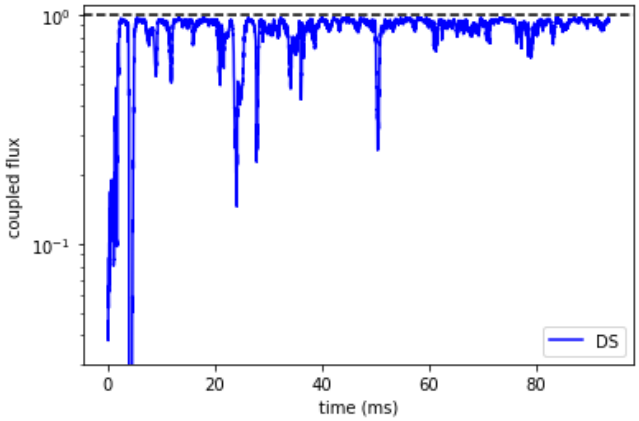

Figure 18. Telecom output intensity in closed loop: E2E simulation with input field amplitude fluctuation and phase variation during modulation and with photometric measurements ($f_c = 12\ kHz$, $f_m = 50\ kHz$, $f_{pm} = 1\ kHz$)

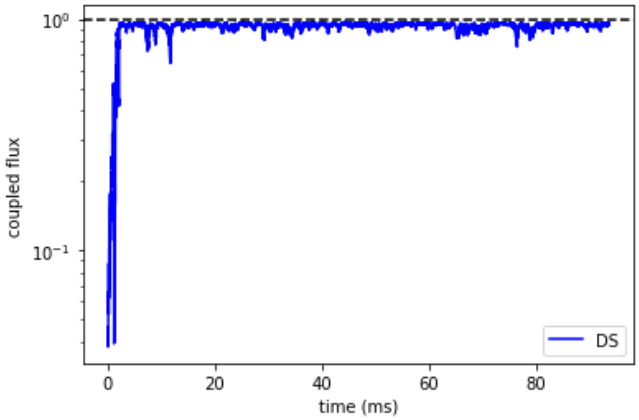

Figure 19. Telecom output intensity in closed loop: E2E simulation with input field amplitude fluctuation and phase variation during modulation and with photometric measurements ($f_c = 12\ kHz$, $f_m = 50\ kHz$, $f_{pm} = 4\ kHz$)

5. CONCLUSION

Coherent combining with a PIC for correcting the effects of turbulence on an optical link present many advantages. However, it requires a PIC with fast phase shifters.

In the control laws described in the literature, the maximum modulation frequency of these phase shifters must be higher and higher as the number of phase shifters increases. The bandwidth accessible with certain PIC and phase shifter technologies is limited, which could constitute a handicap for the implementation of PIC with a high number of degrees of correction.

To overcome this limit, we proposed here a phase estimation method, called spatial diversity modulation, which requires a unique temporal modulation, and therefore a bandwidth independent of the number of modes. We tested this method using numerical modeling. This modeling simulates the effects of atmospheric turbulence on optical propagation, the spatial multiplexer which transforms the wave propagating in free space into a set of guided waves, and finally a PIC whose phase shifters are controlled in a closed loop from the output signals.

We placed ourselves in a representative scenario of a LEO satellite-ground station optical link. We first demonstrated that the simple correction of the phases of the guided waves was sufficient, thus allowing the use of simplified PICs compared to those proposed in the literature. With numerical modeling, we then showed that the phase shifters control based on spatial diversity modulation is able to close the loop and is stable and

presents satisfactory performance with regard to a high-speed optical link. Finally, we showed that adding so-called photometric measurements - the instantaneous power of each guided wave at the PIC input - significantly improved the performance of the loop. We propose a PIC architecture to have these measurements.

The next stage of our work consists of ensuring that the impact of measurement noise on the control loop remains limited. At the same time, we are developing a laboratory experiment to test this method under conditions representative of a real implementation.

APPENDIX A. COHERENT COMBINATION OF TWO BEAMS USING A MZI

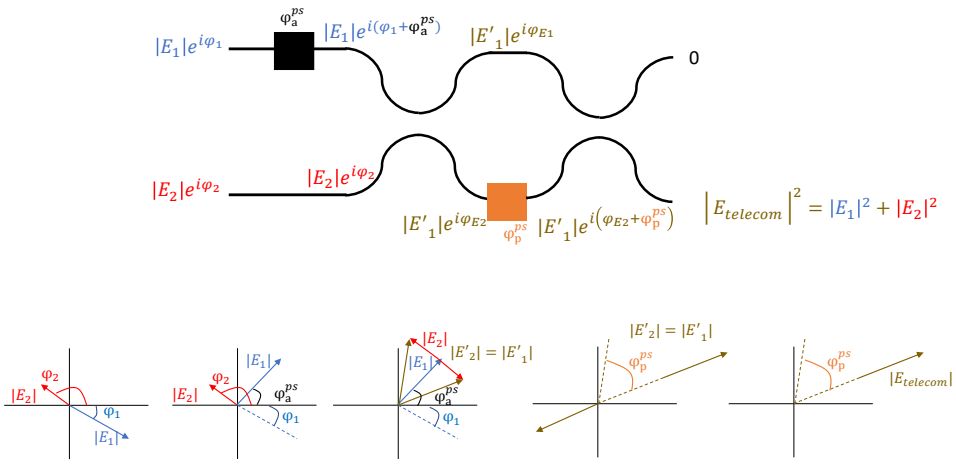

Figure 20. MZI coherent combination principle

APPENDIX B. PSEUDO-SIGNAL (DIFFERENTIAL MEASUREMENTS) DEVELOPMENT

Considering small phase differences $\boldsymbol{\varphi}$, the j^{th} intensity measurement Taylor expansion gives:

$$s_j(\boldsymbol{\varphi}) = s_j(\boldsymbol{\varphi})|_{\boldsymbol{\varphi}=\mathbf{0}} + \sum_k \frac{\partial s_j(\boldsymbol{\varphi})}{\partial \varphi_k}\bigg|_{\boldsymbol{\varphi}=\mathbf{0}} \varphi_k^{res} + \frac{1}{2}\sum_k\sum_l \frac{\partial^2 s_j(\boldsymbol{\varphi})}{\partial\varphi_k\partial\varphi_l}\bigg|_{\boldsymbol{\varphi}=\mathbf{0}} \varphi_k^{res}\varphi_l^{res}, \tag{18}$$

with φ_k^{res} the k^{th} element of the small residual phase $\boldsymbol{\varphi}$. By modulating all phase-shifters simultaneously with the spatial modulation vector, $\boldsymbol{\delta\varphi_m}$, the Taylor expansion becomes:

$$\begin{aligned} s_j(\boldsymbol{\varphi} \pm \boldsymbol{\delta\varphi_m}) =& s_j(\boldsymbol{\varphi} \pm \boldsymbol{\delta\varphi_m})|_{\boldsymbol{\varphi}=\mathbf{0}} + \sum_k \frac{\partial s_j(\boldsymbol{\varphi} \pm \boldsymbol{\delta\varphi_m})}{\partial \varphi_k}\bigg|_{\boldsymbol{\varphi}=\mathbf{0}} (\varphi_k^{res} \pm \delta\varphi_{mk}) \\ &+ \frac{1}{2}\sum_k\sum_l \frac{\partial^2 s_j(\boldsymbol{\varphi} \pm \boldsymbol{\delta\varphi_m})}{\partial\varphi_k\partial\varphi_l}\bigg|_{\boldsymbol{\varphi}=\mathbf{0}} (\varphi_k^{res} \pm \delta\varphi_{mk})(\varphi_l^{res} \pm \delta\varphi_{ml}) \end{aligned}. \tag{19}$$

Then the pseudo-signal becomes:

$$\begin{aligned} \Delta s_j &= \sum_k\sum_l 2\,\frac{\partial^2 s_j(\boldsymbol{\varphi})}{\partial\varphi_k\partial\varphi_l}\bigg|_{\boldsymbol{\varphi}=\mathbf{0}} \delta\varphi_{ml}\varphi_k^{res} \\ &= \sum_k m_{j,k}\varphi_k^{res} \end{aligned}, \tag{20}$$

with $m_{j,k}$ the coefficients of the interaction matrix $\boldsymbol{M}(\boldsymbol{\delta\varphi_m})$ define as:

$$m_{j,k} = \sum_l 2 \left. \frac{\partial^2 s_j(\boldsymbol{\varphi})}{\partial\varphi_k \partial\varphi_l} \right|_{\boldsymbol{\varphi=0}} \delta\varphi_{ml} \,. \tag{21}$$

Then it comes:

$$\boldsymbol{\Delta s} = \boldsymbol{M_{\delta\varphi_m}} \boldsymbol{\varphi^{res}} \,. \tag{22}$$

Equation 20 can be rewritten as follows:

$$\Delta s_j = \boldsymbol{\delta\varphi_m}^t \boldsymbol{T^j} \boldsymbol{\varphi^{res}} \,, \tag{23}$$

with $\boldsymbol{T^j}$ the j^{th} component of the three dimension PIC tensor $\boldsymbol{T^{j,k,l}}$, with $j \in (0, N-1)$ the output intensity measurement number and $k, l \in (0, N)$ the phase-shifters number. $\boldsymbol{T^j}$ is a symmetric matrix.

ACKNOWLEDGMENTS

This work is co-funded by CNES.

This work was supported by the Action Spécifique Haute Résolution Angulaire (ASHRA) of CNRS/INSU co-funded by CNES.

We thank M.Boutiller for our fruitful discussions and L.Paillier for her help using the PILOT code.

REFERENCES

[1] Primmerman, C. A., Price, T. R., Humphreys, R. A., Zollars, B. G., Barclay, H. T., and Herrmann, J., "Atmospheric-compensation experiments in strong-scintillation conditions," *Applied Optics* **34**(12), 2081–2088 (1995).

[2] Barchers, J. D., Fried, D. L., and Link, D. J., "Evaluation of the performance of hartmann sensors in strong scintillation," *Applied optics* **41**(6), 1012–1021 (2002).

[3] Schwartz, N., *Précompensation des effets de la turbulence par optique adaptative: application aux liaisons optiques en espace libre*, PhD thesis, Université Nice Sophia Antipolis (2009).

[4] Rinaldi, L., *Mitigation of atmospheric turbulence effects on optical links by integrated optics*, PhD thesis, Université Paris-Saclay (2022).

[5] Vorontsov, M. A., Carhart, G. W., and Ricklin, J. C., "Adaptive phase-distortion correction based on parallel gradient-descent optimization," *Optics Letters* **22**, 907 (June 1997).

[6] Hu, Q., Zhen, L., Mao, Y., Zhu, S., Zhou, X., and Zhou, G., "Adaptive stochastic parallel gradient descent approach for efficient fiber coupling," *Optics Express* **28**(9), 13141–13154 (2020).

[7] O'Meara, T. R., "The multidither principle in adaptive optics," *Journal of the Optical Society of America* **67**, 306 (Mar. 1977).

[8] Zanetto, F., Grimaldi, V., Toso, F., Guglielmi, E., Milanizadeh, M., Aguiar, D., Moralis-Pegios, M., Pitris, S., Alexoudi, T., Morichetti, F., Melloni, A., Ferrari, G., and Sampietro, M., "Dithering-based real-time control of cascaded silicon photonic devices by means of non-invasive detectors," *IET Optoelectronics* **15**(2), 111–120 (2021). _eprint: https://onlinelibrary.wiley.com/doi/pdf/10.1049/ote2.12019.

[9] Ahn, H. K. and Kong, H. J., "Cascaded multi-dithering theory for coherent beam combining of multiplexed beam elements," *Optics Express* **23**, 12407 (May 2015).

[10] Ma, Y., Zhou, P., Wang, X., Ma, H., Xu, X., Si, L., Liu, Z., and Zhao, Y., "Coherent beam combination with single frequency dithering technique," *Optics Letters* **35**, 1308–1310 (May 2010). Publisher: Optica Publishing Group.

[11] Billault, V., Bourderionnet, J., Leviandier, L., Feneyrou, P., Maho, A., Sotom, M., and Brignon, A., "Evaluation of a multimode receiver with a photonic integrated combiner for satellite to ground optical communications," (2022).

[12] Rinaldi, L., Michau, V., Védrenne, N., Petit, C., Mugnier, L., Lim, C., Montri, J., Paillier, L., and Boutillier, M., "Sensorless adaptive optics for optical communications," in [*Free-Space Laser Communications XXXIII*], Hemmati, H. and Boroson, D. M., eds., 26, SPIE, Online Only, United States (Mar. 2021).

[13] Weyrauch, T., Vorontsov, M. A., Gowens, J., and Bifano, T. G., "Fiber coupling with adaptive optics for free-space optical communication," 177–184 (Jan. 2002).

[14] Labroille, G., Denolle, B., Jian, P., Genevaux, P., Treps, N., and Morizur, J.-F., "Efficient and mode selective spatial mode multiplexer based on multi-plane light conversion," *Optics Express* **22**, 15599 (June 2014).

[15] Mata Calvo, R., Allioux, D., Reeves, A., Billaud, A., Poliak, J., Pinel, O., Kelemu, H. F., Labroille, G., and Richerzhagen, M., "Alternative passive fiber coupling system based on multi-plane light conversion for satellite-to-ground communications," in [*Free-Space Laser Communications XXXII*], Hemmati, H. and Boroson, D. M., eds., 25, SPIE, San Francisco, United States (Mar. 2020).

[16] Birks, T. A., Gris-Sánchez, I., Yerolatsitis, S., Leon-Saval, S. G., and Thomson, R. R., "The photonic lantern," *Advances in Optics and Photonics* **7**, 107 (June 2015).

[17] Norris, B. R. M., Wei, J., Betters, C. H., Wong, A., and Leon-Saval, S. G., "An all-photonic focal-plane wavefront sensor," *Nature Communications* **11**, 5335 (Dec. 2020).

[18] Chang, H., Chang, Q., Xi, J., Hou, T., Su, R., Ma, P., Wu, J., Li, C., Jiang, M., Ma, Y., et al., "First experimental demonstration of coherent beam combining of more than 100 beams," *Photonics Research* **8**(12), 1943–1948 (2020).

[19] Yu, C., Kansky, J., Shaw, S., Murphy, D., and Higgs, C., "Coherent beam combining of large number of pm fibres in 2-d fibre array," *Electronics Letters* **42**(18), 1 (2006).

[20] Xiang, C., Jin, W., and Bowers, J. E., "Silicon nitride passive and active photonic integrated circuits: trends and prospects," *Photonics Research* **10**, A82 (June 2022).

[21] Siew, S. Y., Li, B., Gao, F., Zheng, H. Y., Zhang, W., Guo, P., Xie, S. W., Song, A., Dong, B., Luo, L. W., Li, C., Luo, X., and Lo, G.-Q., "Review of Silicon Photonics Technology and Platform Development," *Journal of Lightwave Technology* **39**, 4374–4389 (July 2021). Conference Name: Journal of Lightwave Technology.

[22] Lin, J., Bo, F., Cheng, Y., and Xu, J., "Advances in on-chip photonic devices based on lithium niobate on insulator," *Photonics Research* **8**, 1910–1936 (Dec. 2020). Publisher: Optica Publishing Group.

[23] Aalto, T., Cherchi, M., Harjanne, M., Bhat, S., Heimala, P., Sun, F., Kapulainen, M., Hassinen, T., and Vehmas, T., "Open-Access 3-μm SOI Waveguide Platform for Dense Photonic Integrated Circuits," *IEEE Journal of Selected Topics in Quantum Electronics* **25**, 1–9 (Sept. 2019). Conference Name: IEEE Journal of Selected Topics in Quantum Electronics.

[24] Mahé, F., *Application d'un modèle atmosphérique à l'étude des fluctuations d'indice de réfraction dans la couche limite: influence de la scintillation sur l'analyse de front d'onde*, PhD thesis, Nice (2000).